Supporting Information

Discovery of Robust Interlocked Ferroelectricity in 2D $AgCrSe_2$ via Chemical Vapor Deposition

Zhongshi Zhang, [a,b] *Jing Xia,** [a, b] *Xuanze Li,* [a, b] *Lifeng Tian,* [a, b] *Suijiang Cai,* [a,b] *Jing Li,* [a, b] *Qing Meng,* [b,c] *Jiangtao Li,* [b,c] *Chang Liu,* [d] *Xiangmin Meng** [a, b]

[a]Key Laboratory of Photochemical Conversion and Optoelectronic Materials, Technical Institute of Physics and Chemistry, Chinese Academy of Sciences, Beijing, 100190, P. R. China.

E-mail: mengxiangmin@mail.ipc.ac.cn; xiajing@mail.ipc.ac.cn;

[b]Centre of Material Science and Optoelectronic Engineering, University of Chinese Academy of Science, Beijing, 10049, P. R. China.

[c]Key Laboratory of Cryogenics, Technical Institute of Physics and Chemistry, Chinese Academy of Sciences, Beijing 100190, P. R. China

[d]Institute for Computational Materials Science, Joint Center for Theoretical Physics School of Physics and Electronics, Henan University, Kaifeng 475004, P. R. China.

Supplementary Note 1. Definition and calculation of effective piezoelectric coefficient d_{33}

Lateral and vertical dual AC resonance tracking (DART) PFM was employed to characterize IP and OOP ferroelectric domains, piezoelectric responses, and the corresponding piezoelectric coefficients.

$$d_{33} = \frac{A}{V_{AC}Q} = \frac{Amp \cdot deflection\ sensitivity}{V_{AC}Q}$$

The amplitude (Amp) represents the measured piezoelectric response magnitude, while the deflection sensitivity and quality factor (Q) are intrinsic parameters of the cantilever probe. In this work, the measured deflection sensitivity and quality factor (Q) are 132 nm/V and 165, respectively. The applied alternating current voltage (V_{AC}) denotes the excitation amplitude used in switching spectroscopy SS-PFM measurements.

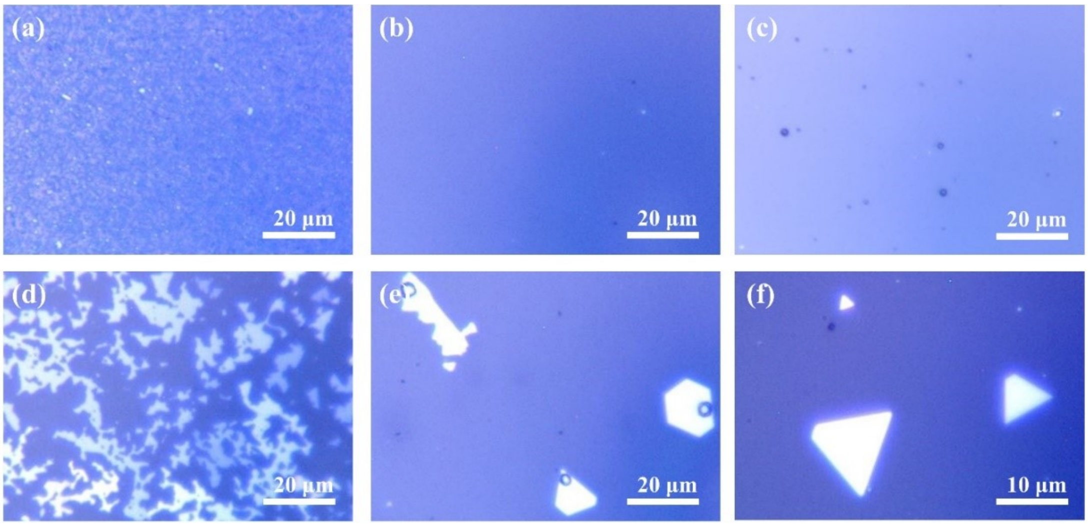

Figure S1. The comparison of OM images for $AgCrSe_2$ nanoflakes synthesized under different growth conditions. a) $AgCrSe_2$ grown on a Si/SiO_2 substrate. b)

OM image without NaCl addition in the precursors. c) Growth results without Cr incorporation in the precursor. d) OM image under an H_2/Ar flow rate of 200 sccm. e) Optical image using unmilled $AgNO_3$ as the precursor. f) OM image synthesized by the Method of **Experimental section**.

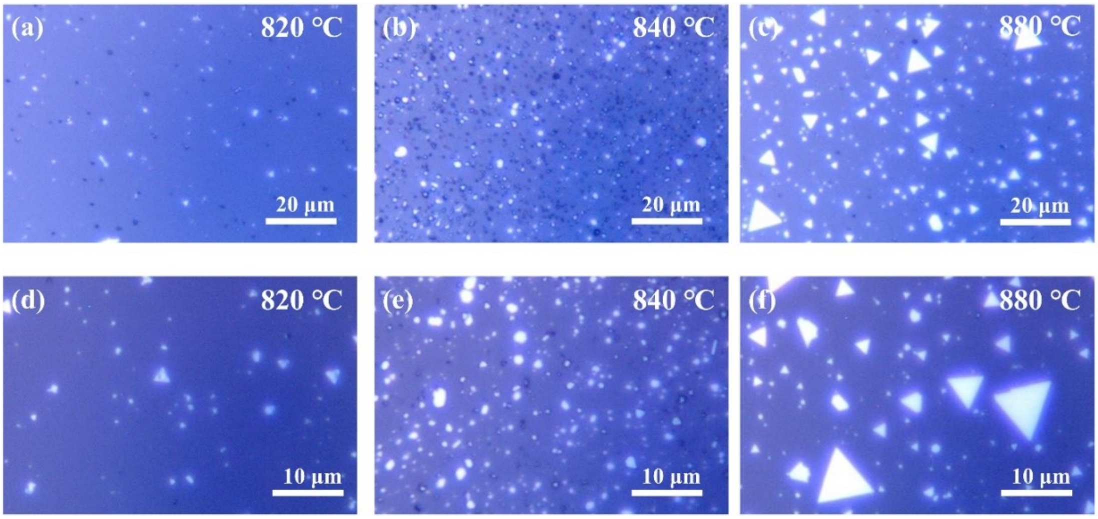

Figure S2. Optical Micrograph (OM) images of $AgCrSe_2$ nanoflakes grown on mica substrate under different temperature conditions (820 – 880 °C). a-c) The spatial distribution of the $AgCrSe_2$ nanoflakes under a 100x objective lens. d-f) The spatial distribution of the $AgCrSe_2$ nanoflakes under a 50x objective lens.

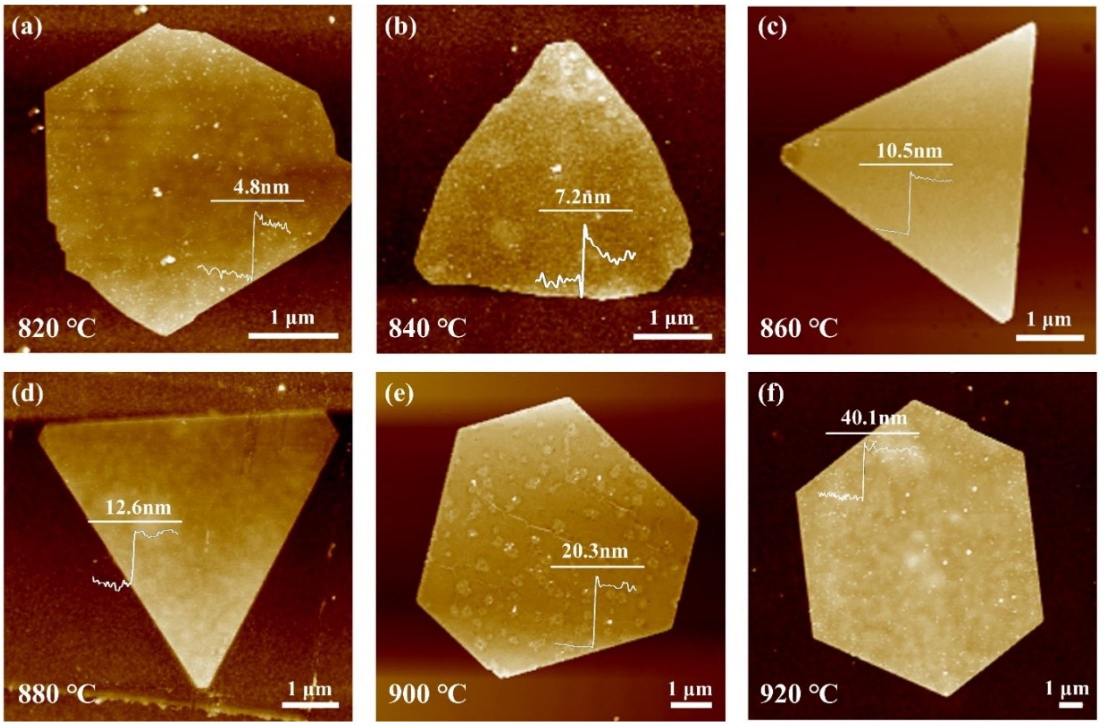

Figure S3. a-f) AFM images of $AgCrSe_2$ samples under different growth temperature conditions (820 – 920 °C).

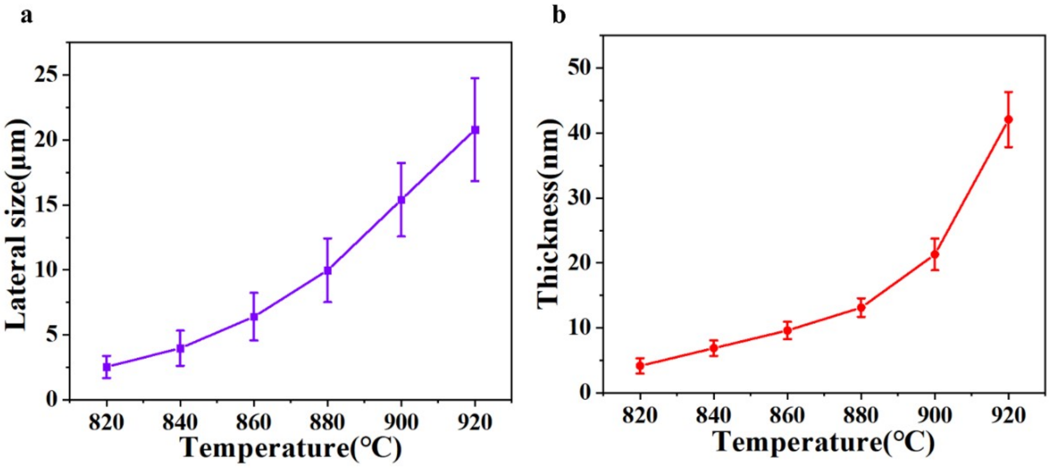

Figure S4. a) Variation of average lateral size of $AgCrSe_2$ nanoflakes under different growth temperature conditions. b) Variation of average thickness in $AgCrSe_2$ nanoflakes under different growth temperature conditions.

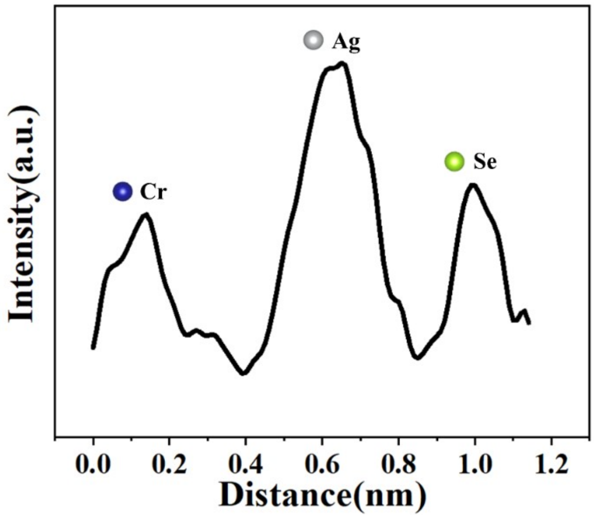

Figure S5. The atomic column intensity distribution of Cr, Ag, and Se in the cross-sectional image.

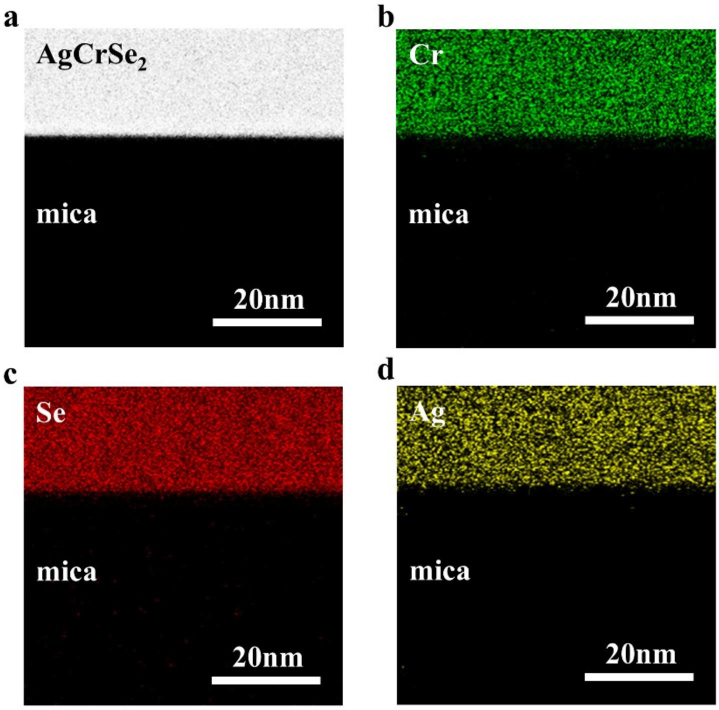

Figure S6. a) Low-magnification HAADF image of the AgCrSe$_2$ cross-sectional sample, with the mica substrate in the background. b – d) Corresponding EDS elemental mapping images for Ag (yellow), Cr (green), and Se (red), respectively.

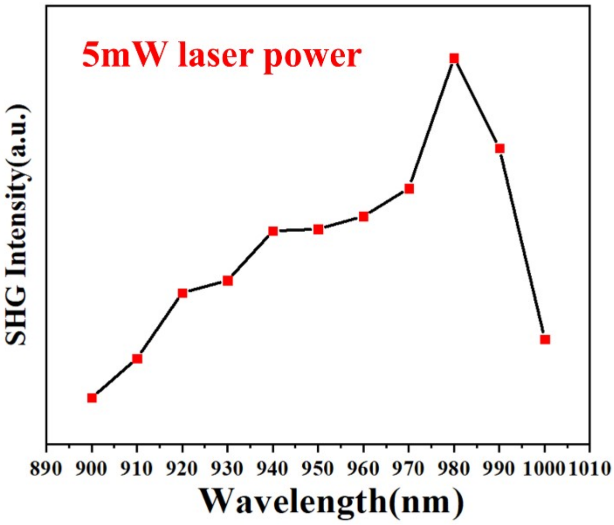

Figure S7. The comparison diagram of SHG intensities for $AgCrSe_2$ nanoflakes under different excitation wavelengths (900 - 1000 nm) with fixed laser power.

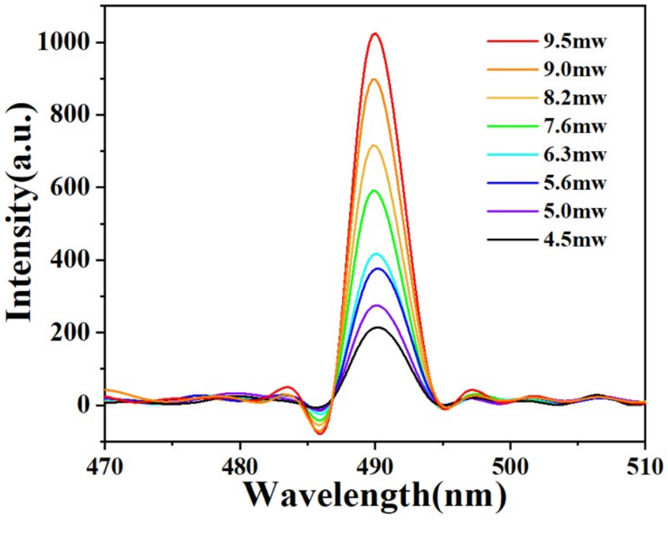

Figure S8. Power-dependent SHG spectra of $AgCrSe_2$ nanoflakes under the excitation wavelength of 980 nm.

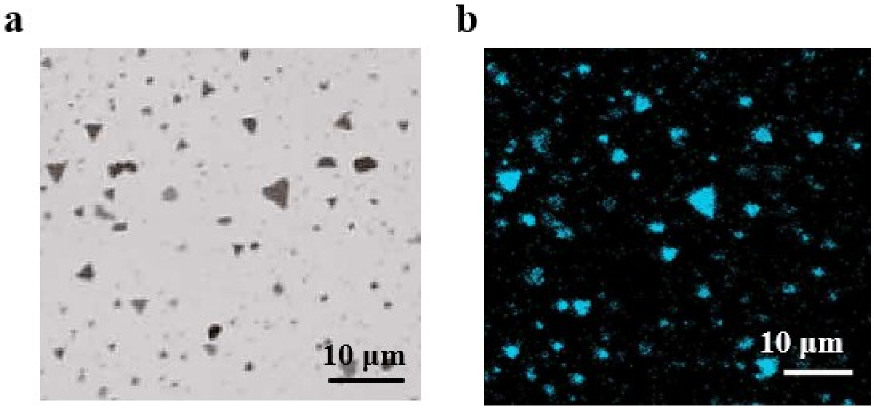

Figure S9. a) Large-area optical micrograph of $AgCrSe_2$ nanoflakes. b) Corresponding large-area SHG mapping image of the same $AgCrSe_2$ nanoflake region shown in (a).

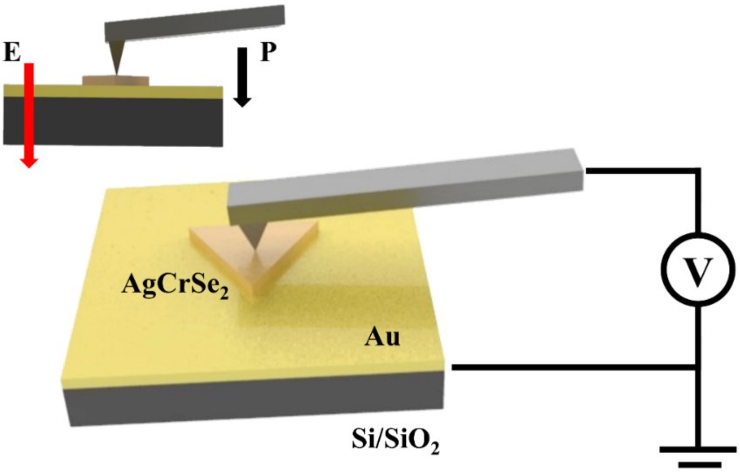

Figure S10. Schematic diagram of the PFM testing setup, with an inset illustrating the magnified side-view schematic of the device.

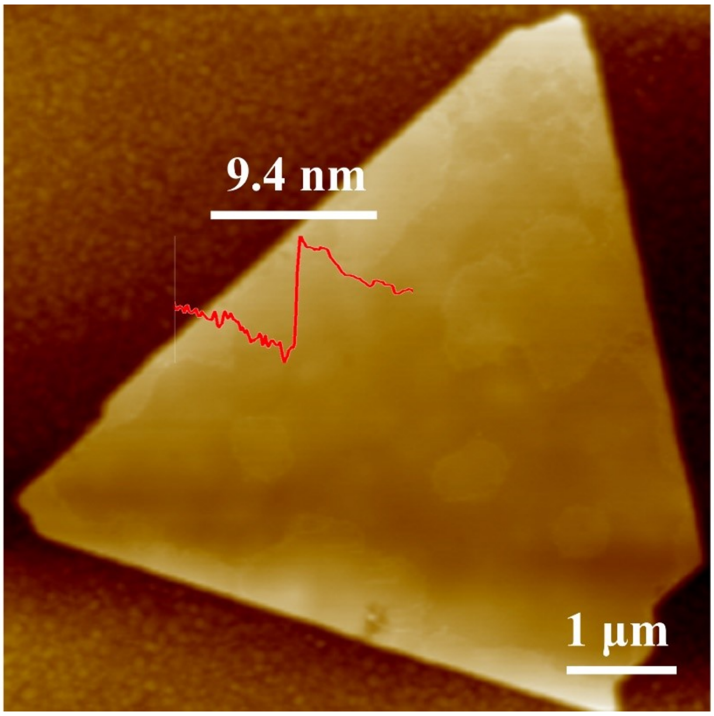

Figure S11. Topography image and thickness (9.4nm) of the $AgCrSe_2$ nanoflake under the OOP and IP measurement mode.

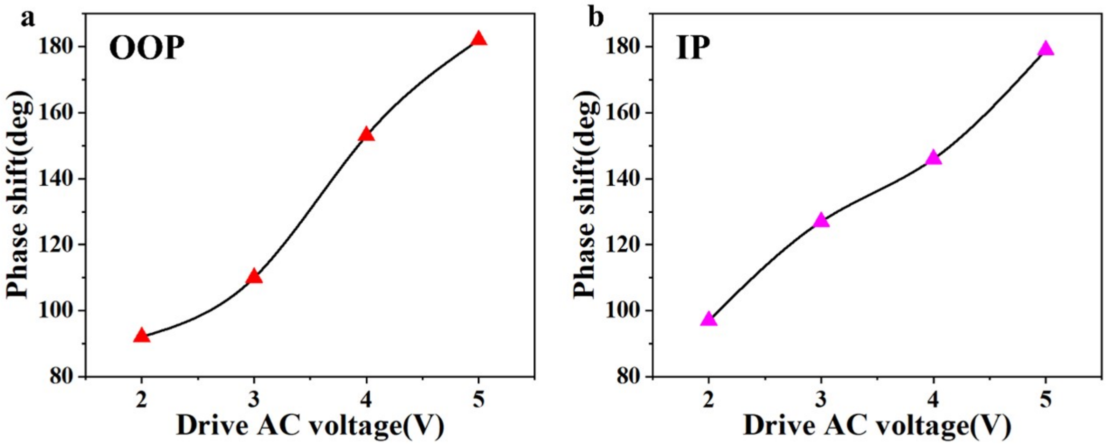

Figure S12. a) Relative phase shift profiles under varying AC voltage bias (±2V - ± 5V) in the OOP orientation. b) Relative phase shift profiles under varying AC voltage bias (±2V - ± 5V) in the IP orientation.

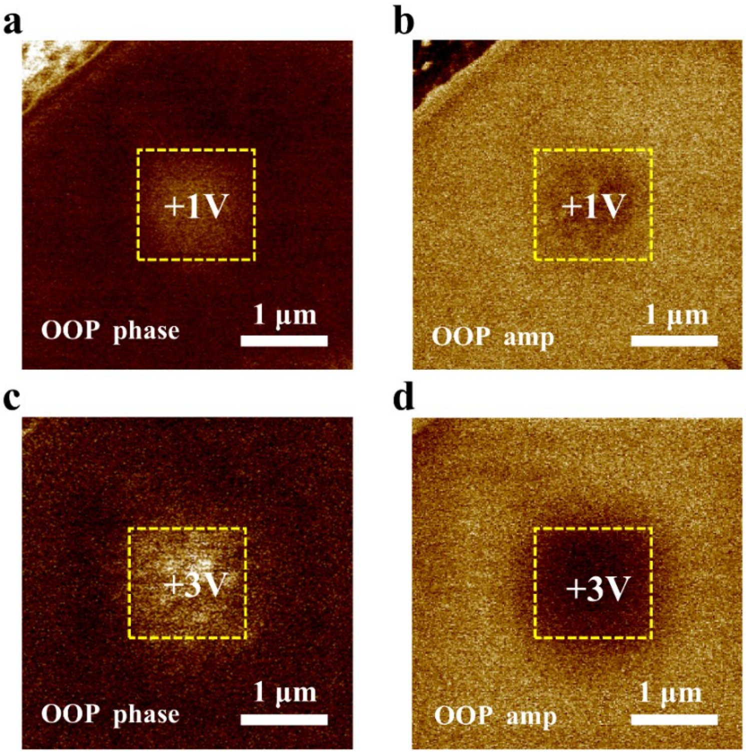

Figure S13. a,b) the phase image and amplitude image in OOP mode under the DC voltage of ±1V. c,d) the phase image and amplitude image in OOP mode under the DC voltage of ±3V.

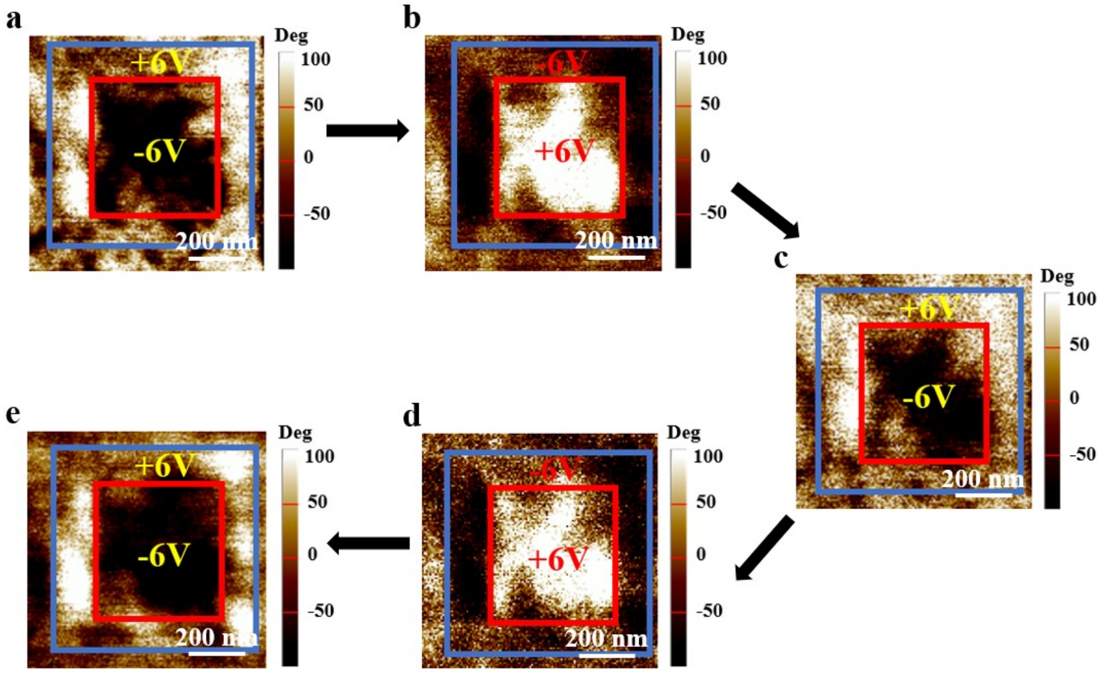

Figure S14. a-e) Polarization endurance test of $AgCrSe_2$ nanoflake in OOP mode under a ± 6 V poling voltage, conducted through five consecutive polarization switching cycles.

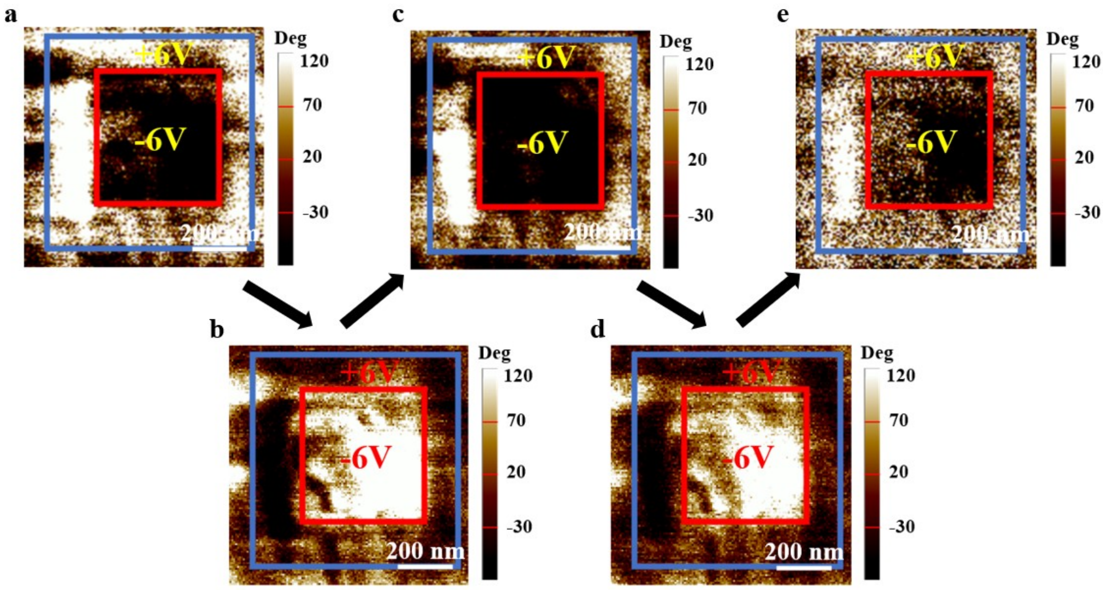

Figure S15. a-e) Polarization endurance test of $AgCrSe_2$ nanoflake in IP mode under a ± 6 V poling voltage, conducted through five consecutive polarization switching cycles.

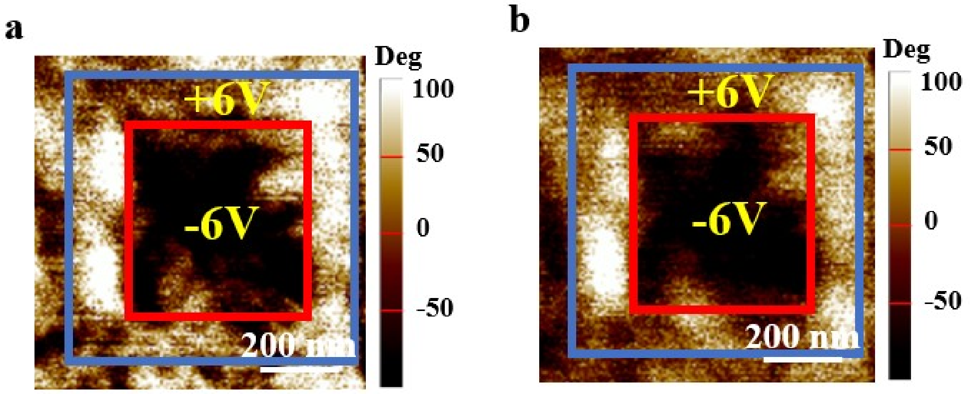

Figure S16. Polarization stability test of $AgCrSe_2$ nanoflake under a ±6 V DC poling voltage of OOP mode: comparison of the (a) initial state and (b) state after 8 hours of continuous polarization.

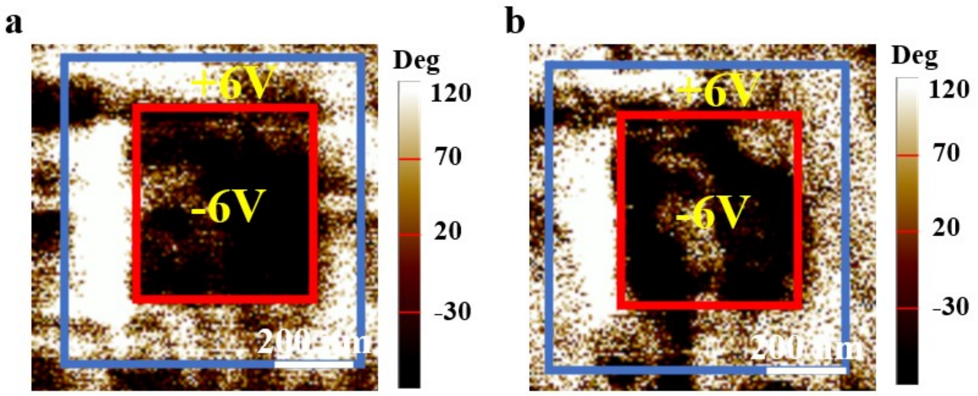

Figure S17. Polarization stability test of $AgCrSe_2$ nanoflake under a ±6 V DC poling voltage of IP mode: comparison of the (a) initial state and (b) state after 8 hours of continuous polarization.

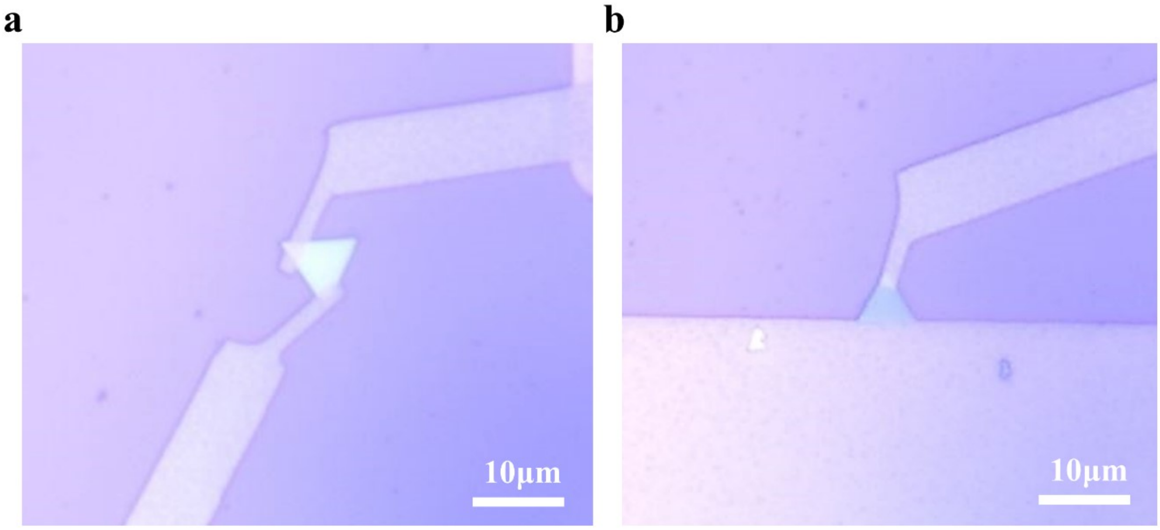

Figure S18. a) OM image of the planar device. b) OM image of the vertical device.

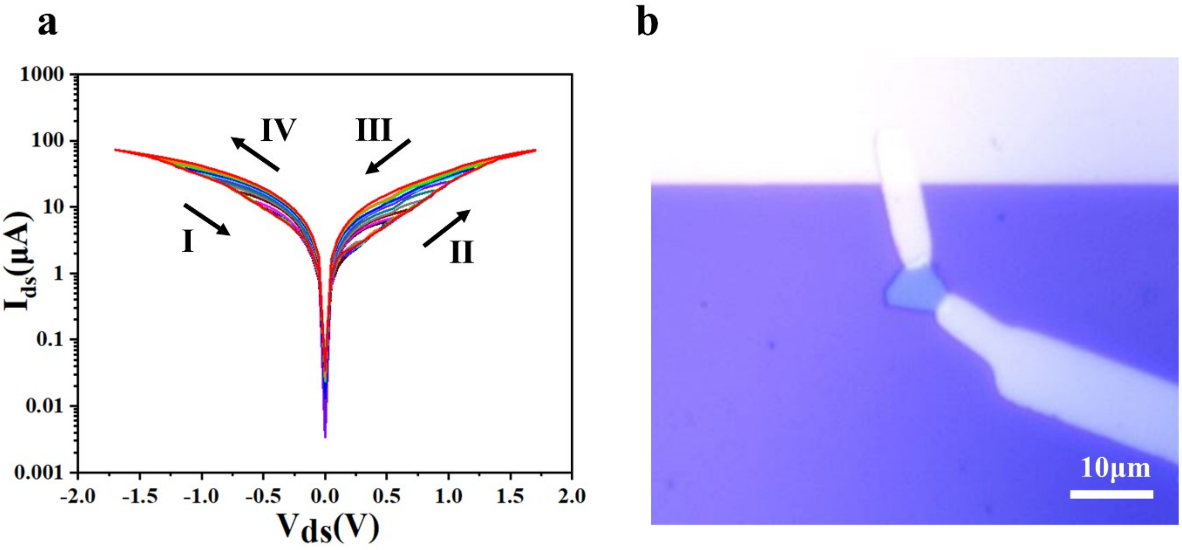

Figure S19. a) Logarithmic-scale I-V curve of a planar device under bias voltages ranging from ±0.5V to ±1.7V. b) OM image of another planar device.

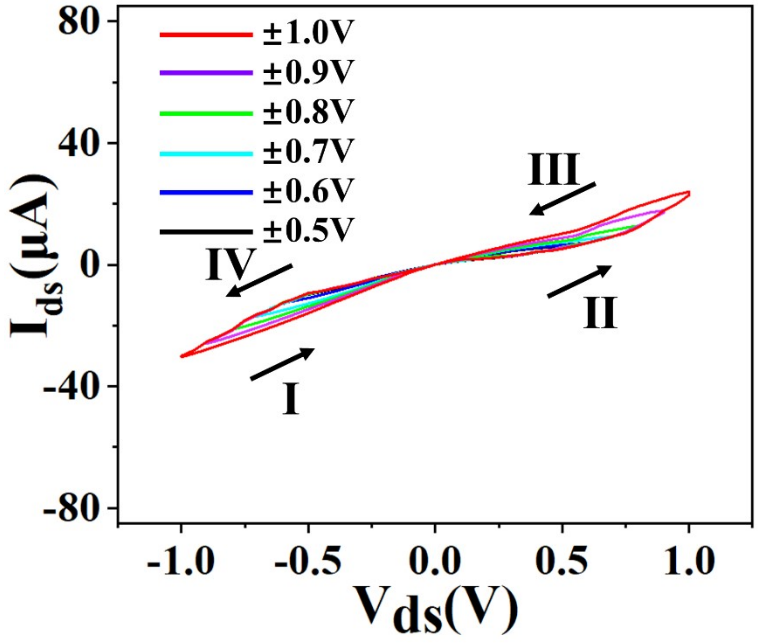

Figure S20. I-V characteristics of planar devices under successive maximum bias voltages.

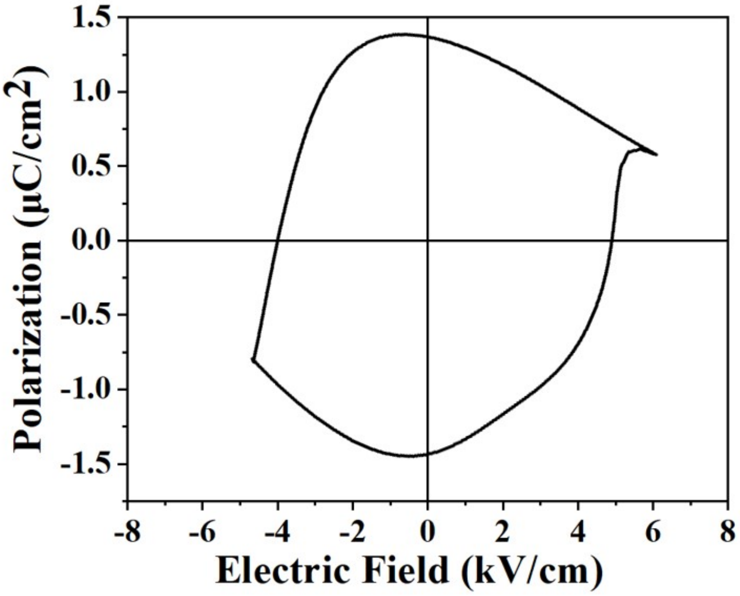

Figure S21. P-E hysteresis loops of $AgCrSe_2$ with the thicknesses of 10nm, showing its robust and intrinsic roomtemperature ferroelectricity.

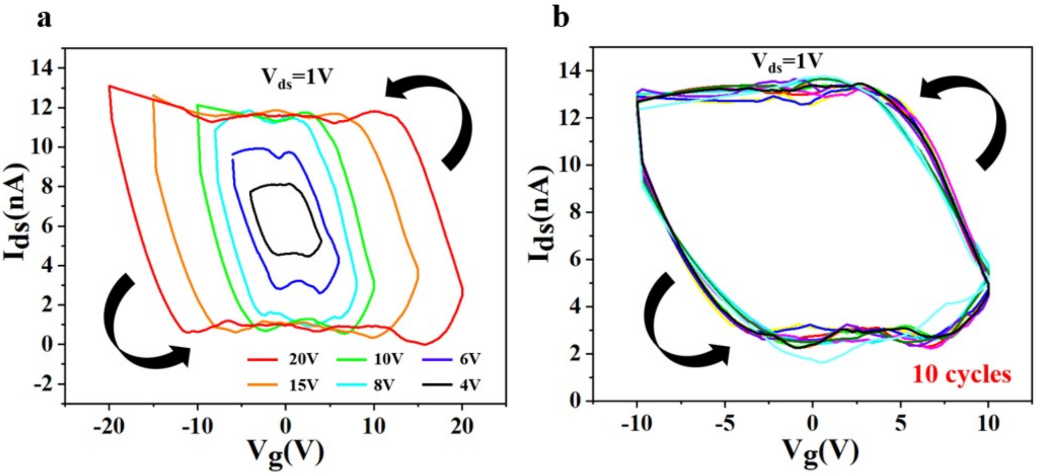

Figure S22. a) Transfer characteristics (V_g-I_{ds} curves) of the Ferroelectric field-effect transistor measured under different gate voltage sweep ranges (from ±4 V to ±20 V) with a constant read voltage (V_{ds} = 1 V). b) Corresponding V_g-I_{ds} curves of the ferroelectric transistor acquired over 10 consecutive cycles under a fixed gate voltage sweep condition (±10 V) and read voltage (V_{ds} = 1 V), demonstrating the cycling stability.

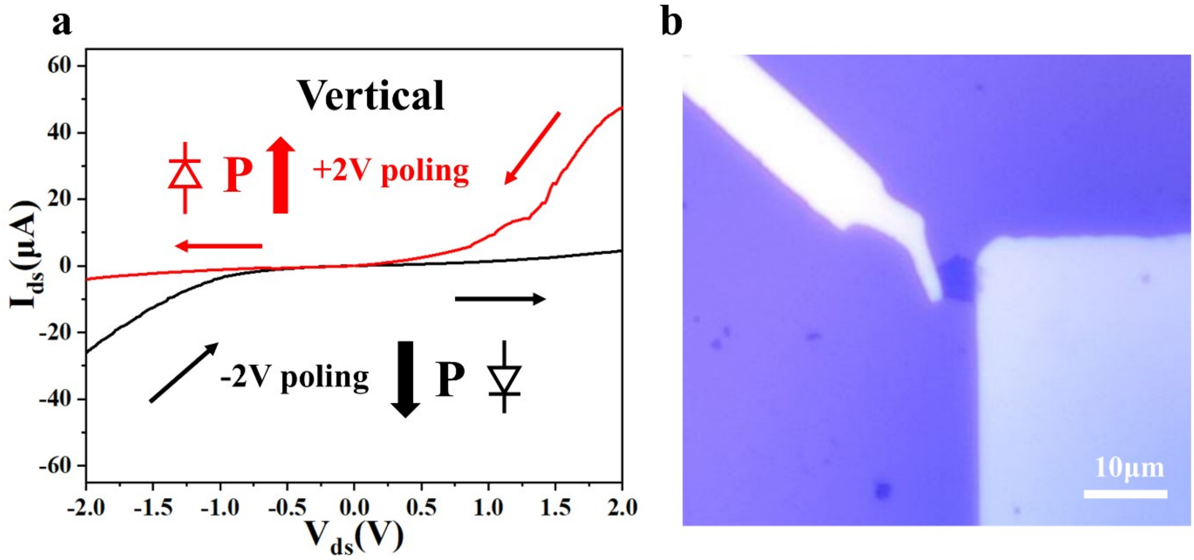

Figure S23. a) I-V curves of vertical $AgCrSe_2$ ferroelectric diode device by applying opposite poling voltage (+ 2 V and − 2 V) b) OM image of another vertical device.

Table S1. Comparative analysis of ferroelectric properties with other reported 2D ferroelectrics.

Materials	Switching barrier(meV/f.u.)	Tc(K)	On/off ratio	Polarization value(μC/cm^2)	Coercive field(kV/cm)	reference
$AgCrSe_2$	360	480	10^2	1.5	5	This work
$CuCrS_2$	320	700	10			1
$CuInP_2S_6$	150	320	10^2	0.59		2,3
$CuCrSe_2$		700	10			4
2H α-In_2Se_3	66		10		1.625	5,6
3R α-In_2Se_3	850	620	10^3	0.92	200	7,8
Te nanowires			Near 10^2			9
$CuScS_2$	240	370				10
BN				0.68	16	11

References:

[1] Xu X, Zhong T, Zuo N, et al. High-T(C) Two-Dimensional Ferroelectric $CuCrS_2$ Grown via Chemical Vapor Deposition [J]. ACS Nano, 2022, 16(5): 8141-9.

[2] Liu F, You L, Seyler K L, et al. Room-temperature ferroelectricity in $CuInP_2S_6$ ultrathin flakes [J]. Nat Commun, 2016, 7: 12357.

[3] Huang S, Shuai Z, Wang D. Ferroelectricity in 2D metal phosphorus trichalcogenides and van der Waals heterostructures for photocatalytic water splitting [J]. Journal of Materials Chemistry A, 2021, 9(5): 2734-41.

[4] Wang P, Zhao Y, Na R, et al. Chemical Vapor Deposition Synthesis of Intrinsic High‐temperature Ferroelectric 2D $CuCrSe_2$ [J]. Adv Mater, 2024, 36(23): 2400655.

[5] Xue F, Hu W, Lee K-C, et al. Room-Temperature Ferroelectricity in Hexagonally Layered α-In_2Se_3 Nanoflakes down to the Monolayer Limit [J]. Adv Funct Mater, 2018, 28(50): 1803738.

[6] Lv B, Yan Z, Xue W, et al. Layer-dependent ferroelectricity in 2H-stacked few-layer α-In_2Se_3 [J]. Materials Horizons, 2021, 8(5): 1472-80.

[7] Jiang Y, Ning X, Liu R, et al. 2D ferroelectric narrow-bandgap semiconductor Wurtzite' type α-In_2Se_3 and its silicon-compatible growth [J]. Nat Commun, 2025, 16(1): 7364.

[8] Wan S, Li Y, Li W, et al. Room-temperature ferroelectricity and a switchable diode effect in two-dimensional α-In_2Se_3 thin layers [J]. Nanoscale, 2018, 10(31): 14885-92.

[9] Zhang J, Zhang J, Qi Y, et al. Room-temperature ferroelectric, piezoelectric and resistive switching behaviors of single-element Te nanowires [J]. Nat Commun, 2024, 15(1).

[10] Xu X, Chen Y, Liu P, et al. General synthesis of ionic-electronic coupled two-dimensional materials [J]. Nat Commun, 2024, 15(1): 4368.

[11] Yasuda K, Wang X R, Watanabe K, et al. Stacking-engineered ferroelectricity in bilayer boron nitride [J]. Science, 2021, 372(6549): 1458-62.